Experimental and Numerical Investigation of Mini-tab Device for Active Flow Control

Sam Bull*, Dami Adeyemi†, Dom Wilson‡

The University of Bath, Bath, Somerset, BA2 7AY, United Kingdom

and

David Cleaver§ and Jon du Bois¶

Volant Autonomy, Bath, Somerset, BA1 1BP, United Kingdom

Summary

The next generation of aircraft are likely to exhibit a breadth of aeromechanic and aeroelastic behaviors that will be exacerbated by the turbulent flows generated in urban environments. Exploitation of novel flow control technologies will be critical in offering greater control authority to enable this new generation of aerial vehicles for faster, safer, and more efficient flight. This study experimentally investigates the efficacy of a mini-tab active flow control device using a novel dynamic test rig. Under steady conditions, the mini-tab response exhibited non-linearity with deployment height. Under dynamic conditions, the lift and pitching moment displayed hysteresis around their quasi-steady counterpart at low reduced frequencies ($k = 0.05$) but displayed significant deviations at mid to high reduced frequencies (k = 0.15 to 0.31) due to the formation of a tab vortex that propagates downstream. It was demonstrated, for the first time experimentally, that mini-tab dynamic performance is insensitive to unsteady airfoil motions in pitch and plunge – representative of flutter onset. Finally, an existing mini-tab model was extended to capture vortex formation on the upper and lower airfoil surfaces and modified to incorporate mini-tab rate-dependence on vortex initiation. The model showed good agreement with experimental data in both periodic and transient scenarios.

Nomenclature

Experiment

α	=	angle of attack, degrees
c	=	chord length, m
ΔC_l	=	change in lift coefficient due to tab
ΔC_m	=	change in quarter-chord pitching moment coefficient

* Lecturer (Assistant Professor), Mechanical Engineering; scb72@bath.ac.uk
† Research Associate, Mechanical Engineering
‡ PhD Researcher, Mechanical Engineering
§ CEO
¶ CTO

ΔC_N = normal force contribution of tab vortex
h = tab deployment height, m
f = frequency, *Hz*
k = reduced frequency, $\pi fc/U_\infty$
s = reduced time, $t\frac{2U_\infty}{c}$
t = time, sec
U_∞ = freestream velocity, m/s
x/c = normalized chordwise location
y/c = normalized plunge position

Model

A = model constant
β^γ = compressibility correction factor
b = model constant
C = model constant
D = deficiency function
L_{arm} = pitching moment lever arm
M = Mach number
n = model constant
T = vortex time constant
V_f = vortex function

Subscripts

circ = circulatory term
eff = circulatory term
ini = vortex initiation term
0 = mean angle of attack
MT = normalized about reference mini-tab height
qs = quasi-steady
vtx = *vortex term*

Superscripts

+ = rate (time derivative)
e = experiment
eff = effective
ini = vortex initiation
n = iteration number
m = model
te = trailing-edge

I. Introduction

The Urban Air Mobility (UAM) market is growing rapidly. Market frontrunners reveal a range of novel aircraft configurations [1] that are likely to exhibit a breadth of unusual aerodynamic behaviors that will be exacerbated by the turbulent, gusty flows generated in urban environments. Key areas of concern are aeromechanic and aeroelastic instabilities - such as Dutch-roll oscillations [2], vortex ring state [3] and whirl flutter [4] - that can compromise flight safety, cause structural damage, and limit flight envelopes. Exploitation of novel flow control technologies will be critical in offering greater control authority to enable this new generation of aerial vehicles for faster, safer, and more efficient flight.

Flow control methods can be delineated into two groups – passive and active. Passive control methods require no external energy input and are attractive due to their simplicity in operation and integration. Such methods can facilitate UAM vehicle flight through Gurney flaps [5] and deflected propulsor slipstreams [6] for increased wing lift in the conversion corridor, leading-edge tubercules to improve wing-nacelle-propellor interactions [7], and aeroelastic tailoring for augmenting whirl flutter boundaries [8],[9]. Despite their simplicity, however, the benefits of passive control devices are often limited and generally lack broad performance increases [10]. Active flow control techniques on the other hand require exogenous input and provide a powerful alternative to passive control as they can

offer more extensive and significant performance gains. Pulsed blowing [11], synthetic jets [12], and plasma actuation [13] at critical frequencies can exploit natural flow instabilities for efficient control of flow separation. Active flow control devices are also highly suited to aeromechanic and aeroelastic control, where surface and Coandă jets [14],[15], and dynamic Gurney flaps/Micro-Trailing Edge Effectors [16],[17] have demonstrated their efficacy for gust load alleviation and flutter control. In this study, whirl flutter is used as a motivation and basis for the investigation of an active mini-tab device and as such, a brief overview of whirl flutter, its suppression through active control, and mini-tab aerodynamics will be provided.

Whirl flutter is an aeroelastic instability that occurs when propellor/proprotor aerodynamic loads couple with the flexible modes of the wing-nacelle system - and is particularly prevalent on tiltrotor configurations due to the inherent flexibility in the rotor tilting mechanism [18]. This coupling is gyroscopic in nature and can exhibit negative damping beyond critical flight speeds. The occurrence of whirl flutter can lead to unstable vibrations and catastrophic damage to the aircraft which has led to tiltrotors requiring overly thick wings to compensate [19], increasing drag and structural mass. Active flow control techniques can stabilize unstable modes through controllable aerodynamic loads, thereby relaxing wing stiffness constraints and increasing maximum forward flight speeds.

Early investigations focused on active control of the rotor cyclic input to suppress whirl flutter through rotor/wing motion feedback [20],[21]. This was found to increase the damping of critical wing modes, highlighting the coupled nature of the wing-nacelle-rotor system. More recent investigations have probed the effectiveness of actuation strategies outside the rotor system. Numerical work by Hathaway and Gandhi [10] demonstrated successful wing flaperon control of the Bell XV-15, increasing the maximum flight speed by 50 kn - whilst Dong & Li [22] employed a wing mounted aileron to increase the maximum flight speed by 80 kn. Loads control on the main wing can stabilize the wing-nacelle-rotor system during whirl flutter and the investigation into new wing-mounted flow control devices remains a promising avenue.

Ongoing research at The University of Bath [23],[24] is investigating the efficacy of a small control surface called a mini-tab (micro-tab/flow fence) that offers considerable aerodynamic load augmentation for small deployment amplitudes through flow separation. This has two advantages over wing flaperon control. Firstly, due to the relatively low mass, the mini-tab has a higher bandwidth and faster response time. Secondly, the mini-tab is a separate entity to the main flight control surfaces

and thus avoids any saturation issues associated with different trim states in the flight envelope. We envision that such a stand-alone device would be easier to certify.

Dynamic mini-tab performance has been investigated both experimentally and numerically for use in wind turbine and rotorcraft applications [25]-[30]. Findings highlight their potential control authority in terms of load augmentation and response times, but also emphasize regions of adverse performance when positioned further upstream from the wing's trailing-edge due to the formation of a coherent vortical structure. Most of the research to date has focused on mini-tab placements between $x/c = 0.9 - 1.0$, where adverse performance is minimised. However, volumetric constraints within the wing could force any realizable mini-tab solution further from the trailing-edge. In addition, this study keeps the XV-15 tilt rotor aircraft in mind. This aircraft has a flaperon extending across the full wingspan that is hinged around $x/c = 0.75$, which places a constraint on the maximum chordwise placement of any mini-tab device.

Despite the seminal work to date, a full understanding of mini-tab performance in unsteady conditions is still lacking. For active whirl flutter control the source of unsteadiness consists of multi-degree of freedom wing kinematics, along with external disturbances from gusts and turbulence. This study will therefore focus on the unsteady aerodynamics of a mini-tab device at a chordwise position of $x/c = 0.75$ on static and dynamic wings, along with modelling efforts to capture the complex flow physics the system exhibits. Though whirl flutter has been chosen as the basis for this study, the results are relevant to any scenario where dynamic augmentation of wing loading would be beneficial.

II. Methods and Techniques

A. Experimental Setup

Experiments were conducted on The University of Bath's **T**est **R**ig for **U**nsteady aero**DY**namics (**TRUDY**). This is a novel, hydraulically powered, three degree-of-freedom rig capable of large amplitude, high-frequency wing motion coupled with highly unsteady mini-tab deployment.

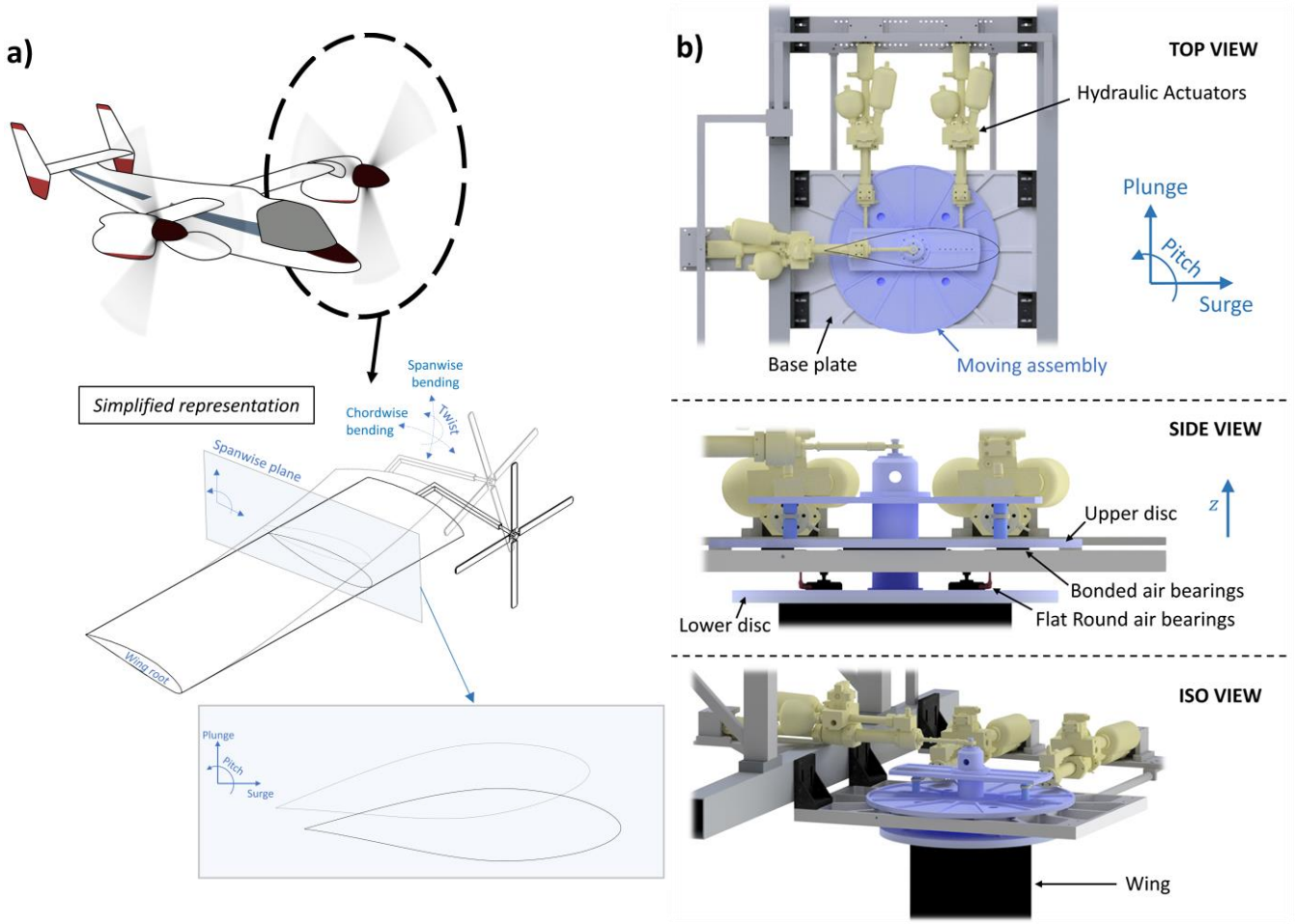

Figure 1: a) Degrees of freedom for tiltrotor wing/propeller system and representative 2D planar motion, b) CAD renderings of TRUDY - TOP VIEW, SIDE VIEW, ISO VIEW.

The design starts from a simplified representation of a tilt rotor wing/propeller assembly in airplane mode, as shown in Figure 1a. In this representation, the propeller is connected to a flexible finite wing structure that is fixed at the root. During whirl flutter modes, the wing will deform in three degrees of freedom, namely spanwise and chordwise bending, and twist. This experimental study considers a 2D representation of this system. If a plane is taken at a spanwise point, the wing deformations can be approximated by two rectilinear translations (plunge, surge) and one rotation (pitch) of the wing airfoil. These are the degrees of freedom the experimental rig can produce. CAD images of the experimental rig are presented in Figure 1b. The moving assembly (blue) is constrained to the pitch, plunge, and surge degrees of freedom (TOP VIEW) through a set of New Way® Bonded and Flat Round air bearings – which use pressurized porous graphite to generate a thin, stiff cushion of air ($\sim$5 µm) between the bearing and operating surface (the moving assembly). These air bearings can be seen in the SIDE VIEW. Four Bonded air bearings are bonded into pockets in the base plate and supply pressure beneath the upper disc, generating a force in the $+z$ direction to support the weight of all moving elements of the rig. A set of four, Flat Round air bearings are then used to provide a force in

the $-z$ direction on the lower disc to constrain the moving assembly in the z axis, whilst providing additional stiffness to the root of the wing model (ISO VIEW). Three Moog hydraulic servo-actuators (yellow) control the moving assembly in three degrees of freedom - plunge, surge, and pitch (TOP VIEW). The wing is mounted underneath the moving assembly (ISO VIEW), hanging vertically into the wind tunnel test section, spanning from floor to ceiling. An airfoil overlay can be seen in the TOP VIEW which represents the wing cross-section projected upwards through the moving assembly. Required actuator extensions/contractions are calculated from inverse kinematics of the wing plunge, surge, and pitch demands, which are then implemented via closed-loop proportional-integral control on the position signals with velocity feedforward and differential cylinder pressure feedback.

Figure 2a presents the airfoil/mini-tab system considered in this study. The airfoil is a NACA 64A-223 to match the XV-15 wing. A simple rotation mechanism is used for mini-tab deployment, where the tab is situated 125 mm from an axis of rotation. In the experiment, the wing has a chord length, c, of 0.5 m, and a length of 1.5 m which spans between the tunnel ceiling and floor to enforce quasi-2D conditions, see Figure 2b. A 15 mm ($0.03c$) gap was maintained between the wing tip and floor to allow for wing motion. Wing construction necessitated the mini-tab mechanism to be split into three identical assemblies that each covered approximately 0.5 m of wingspan. Each tab assembly was driven by a maxon EC60 brushless motor. The mini-tab can deploy dynamically up to a normalized deployment height of $h/c = 0.02$ at 15 Hz. Note that the rotation mechanism will result in a small chordwise change in deployment position ($< 0.001c$). All tests were performed using the University of Bath's Large Wind Tunnel, in the 1.52 x 2.13m (5 by 7 foot) test section, between 30 and 31 m/s, giving a chord-based Reynolds number of 1×10^6.

B. Load Measurements

Lift, quarter-chord pitching moment and unsteady surface pressure measurements were obtained at the mid-span position (Figure 2c) through 41 Honeywell TruStability HSC PCB mounted pressure transducers rated at ±60 mbar, with an I2C digital interface logging at a rate of 1 kHz. Internal tubing connecting the pressure sensors to the wing surface pressure tap was kept to a minimum (< 60 mm). This tubing length has been deemed acceptable by measuring the frequency response to a periodic pressure source [31]. Periodic load and pressure measurements are presented as a phase average of 50 periods of the raw data, whilst measurements during transient motion are presented as an ensemble average of 15 repeats.

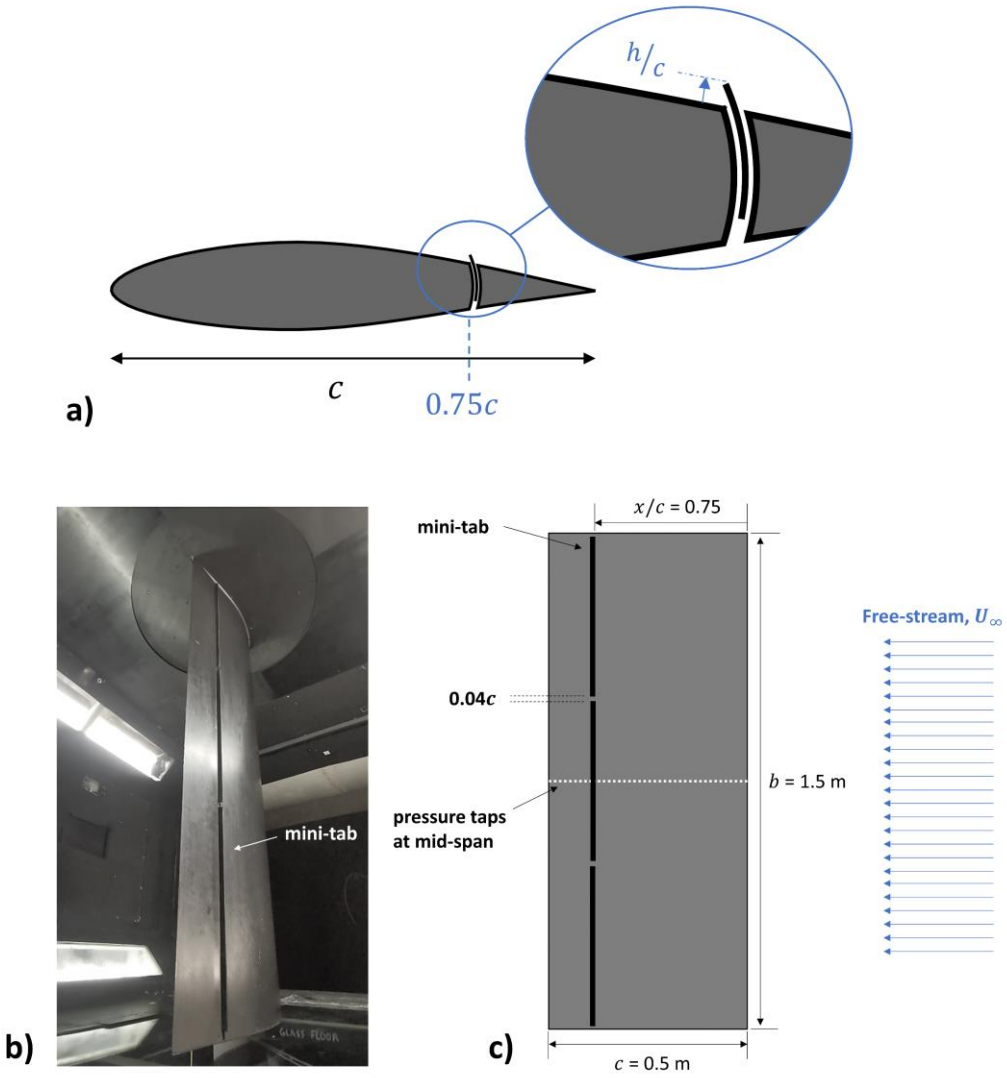

Figure 2: a) NACA 64A-223 airfoil and mini-tab geometry, b) wing with deployed mini-tab mechanisms inside tunnel test section, c) plan-view diagram of wing system.

III. Experimental Results

A. Static performance

To assess the static performance of the mini-tab, the change in lift, ΔC_l, and pitching moment, ΔC_m, were calculated with respect to no tab deployment ($h/c = 0$). Figure 3 shows ΔC_l (a) and ΔC_m (b) for two deplomentstrategies – continuous and discrete at $\alpha_0 = 0^o$. In continuous operation, the mini-tab was deployed sinusoidally for a single cycle at a frequency of 0.01 Hz. Data was then averaged in 500 bins across the deployment range to give a smooth tab performance. Discrete operation is where the tab was commanded to a set height, and data was logged and averaged over 30 seconds. The two are in agreement, which enables the continuous approach for efficent tab characterisation to facilitate reduced-order modelling (Section IV). In general, the mini-tab monotonically decreases the lift and

increases the pitching moment as it is deployed on the upper surface ($h/c > 0$) – and vice versa for deployent on the lower surface. A distinct non-linear region can be observed at low tab heights ($|h\ /\ c| < 0.005$) where the performance plateaus, and even shows slight reversal in behavior. This is a documented issue with mini-tab devices situated upstream from the trailing-edge. A critical height is requried to separate the flow, below which the flow will reattach to give an increase in effective wing camber [32], opposing the intended effect of deployment. At large tab heights, $|h\ /\ c| > 0.01$, the tab separates the flow over the aft portion of the chord. This is shown in Figure 3c for $h/c = -0.02$, where a low magnitude, near-constant pressure is visible behind the deployed tab on the lower surface. In addition, the tab produces a local high-pressure region and augments the upstream pressures relative to $h/c = 0.00$ (Figure 3d). When geometric angle of attack is varied, $\alpha_0 = -4°$ and $+4°$, the mini-tab displays minor variations in ΔC_l and ΔC_m (Figure 3a and 3b) but still retains the same trends. This is promising as the tab performance is relatively insensitive to moderate variations in static geometric angle of attack - e.g. around a trim state.

B. Dynamic performance

To assess unsteady performance, the mini-tab was deployed sinusoidally across a range of amplitudes, h/c, and reduced frequencies, k. The reduced frequency is a non-dimensional frequency that represents the ratio of two time scales - the period of oscillation and the time taken for a parcel of fluid travelling at freestream velocity to travel one chord length. It is defined as

$$k = \frac{\pi f c}{U_\infty} \tag{1}$$

where f is the frequency of oscillation, c is the chord length and U_∞ is the freestream velocity. From stability margin data of the XV-15 by Acree *et al.* [33] we estimate whirl flutter to occur between $k = 0.10$ to 0.20, hence the reduced frequencies tested were $k = 0.025, 0.05, 0.10, 0.15, 0.20$ and 0.31, with demanded tab amplitudes of $h/c = 0.004, 0.008, 0.011, 0.015$. A subset of reduced frequencies at $k = 0.05, 0.15$ and 0.31 are presented in this article, as these capture the key features in the lift, pitching moment and surface pressure measurements. The mini-tab mechanisms were tuned using Maxon's auto-tuning capabilities to give a best fit controller for step demands. As such, there is a slight overshoot in mini-tab amplitude at higher harmonic frequencies. Nevertheless, salient information of performance can still be deduced, and the breadth of data will be more than sufficient for model development – whilst providing the numerical community with a rich data set for code and model validation.

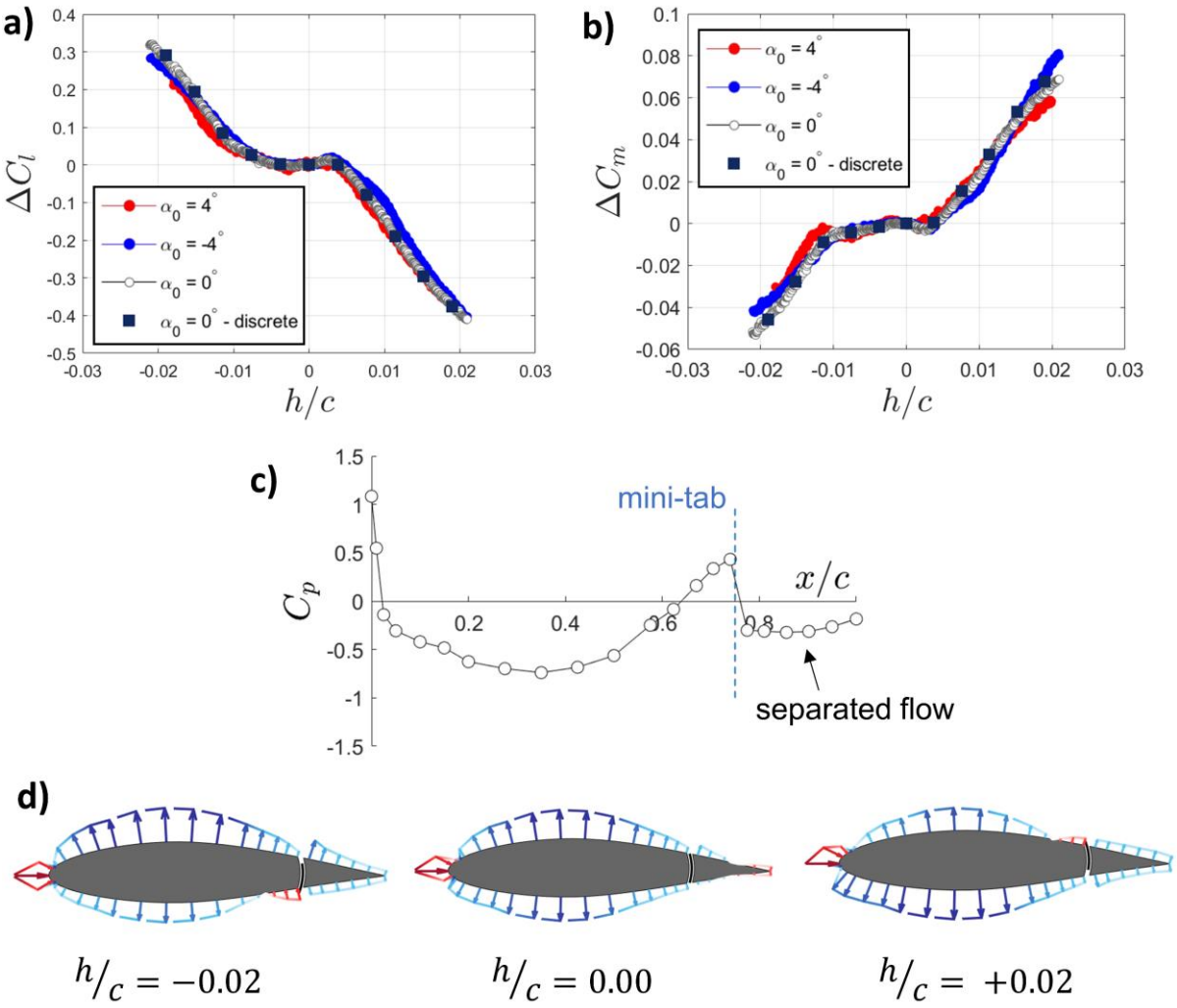

Figure 3: Static performance - a) Change in lift, b) change in pitching moment, c) lower surface pressure at $h/c = -0.02$, and d) pressure distributions at $\alpha_0 = 0^o$.

Figure 4 presents the change in lift, ΔC_l, and pitching moment, ΔC_m, for periodic tab motion across a range of amplitudes and reduced frequencies. Loops of ΔC_l are in a clockwise direction, whereas the loops of ΔC_m are in an anti-clockwise direction. The static performance data is also underlaid for reference. At $k = 0.05$ the loops of ΔC_l and ΔC_m exhibit small hysterises around the underlying quasi-static behavior. At the lowest amplitude, $h/c = 0.004$, the mini-tab generates little aerodynamic change as it is below the critical height needed for flow separation. As k is increased to 0.15, the loops display wider hysteresis, with the emergence of deviations in the loop shape around the maximum h/c which oppose the quasi-static behvaiour. The distortions are accentuted with an increase in reduced frequency to $k = 0.31$, and are particularly pronounced in the ΔC_m loops. As the tab is deployed the pitching moment displays a sharp excursion before rapidly recovering to the quasi-steady value. This reversal in performance at high reduced frequencies is of equal and opposite

magnitude to the quasi-static behavior. Previous studies link the onset of adverse performance to the formation of an aft-tab vortex that convects to the trailing-edge. To corroborate this, select pressure data were extracted for $k = 0.31$ at $h/c = 0.018$ and plotted around the NACA 64A-223 airfoil - see Figure 5.

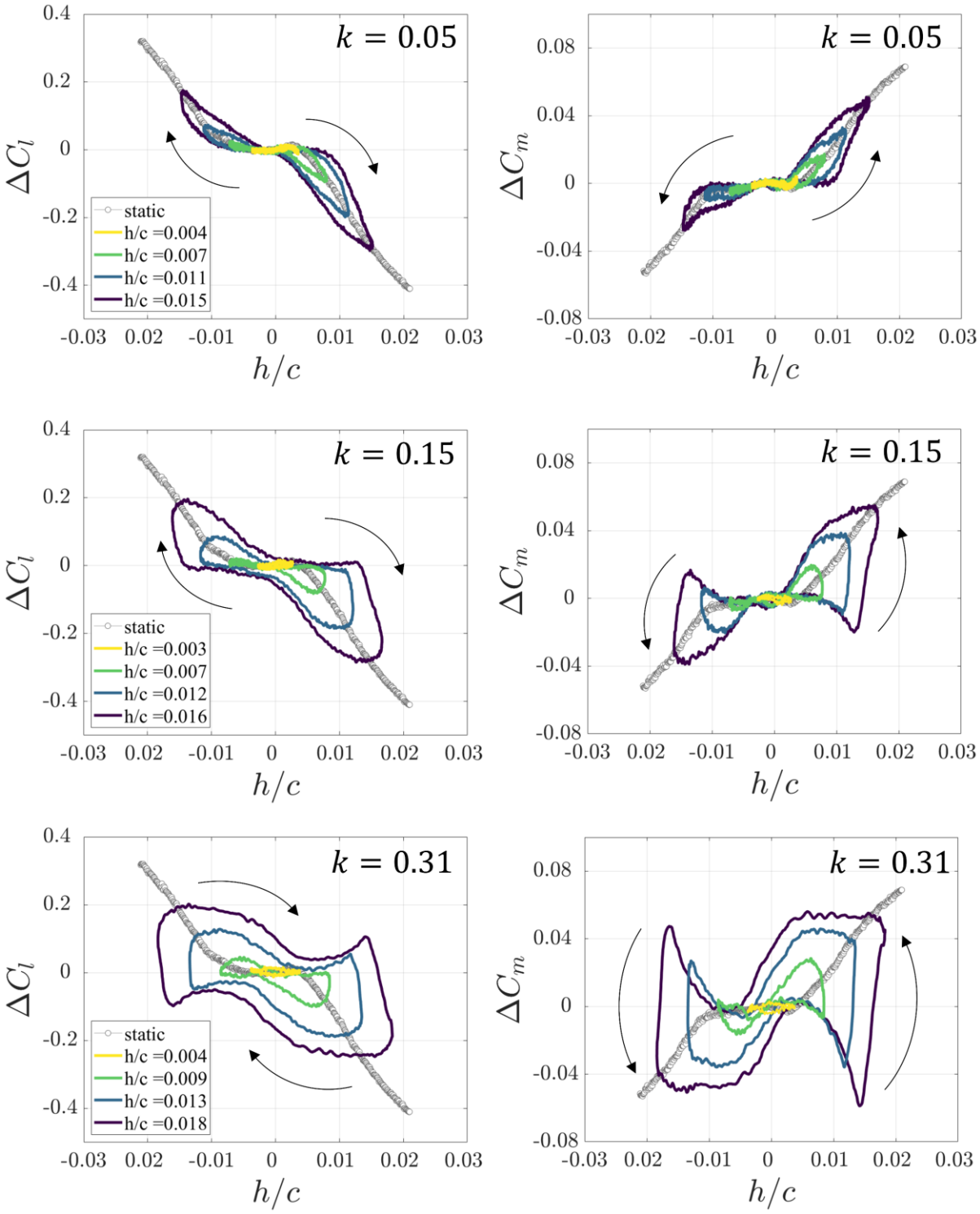

Figure 4: Dynamic mini-tab deployment at selected amplitudes, h/c, and reduced frequencies, k (at $\alpha_0 = 0°$).

As the mini-tab breaks past the critical tab height, $h/c \approx 0.005$, vortex formation is inititated – marked by a distinct decrease in pressure directly behind the tab. At $h/c = 0.012$, the pressure distribution indicates vortex growth and convection through a low-pressure zone spreading towards the trailing-edge. This is reinforced by the sharp decrease in pitching moment and increase in lift. Both ΔC_l and ΔC_m reach their extrema at $h/c = 0.0144$, where the low-pressure zone covers the entire aft portion of the chord on the upper surface. This marks the end of the shedding process. Vieira and Maughmer [32] note that the peak loads are coincident with the arrival of the tab vortex at the trailing-edge, beyond which the vortex is shed into the wake. At maximum tab height the vortex effects have completely decayed, and fully separated flow is shown clearly by the near-constant pressure distribution. Similar observations are made when the tab is deployed on the lower suface, though with opposite effect.

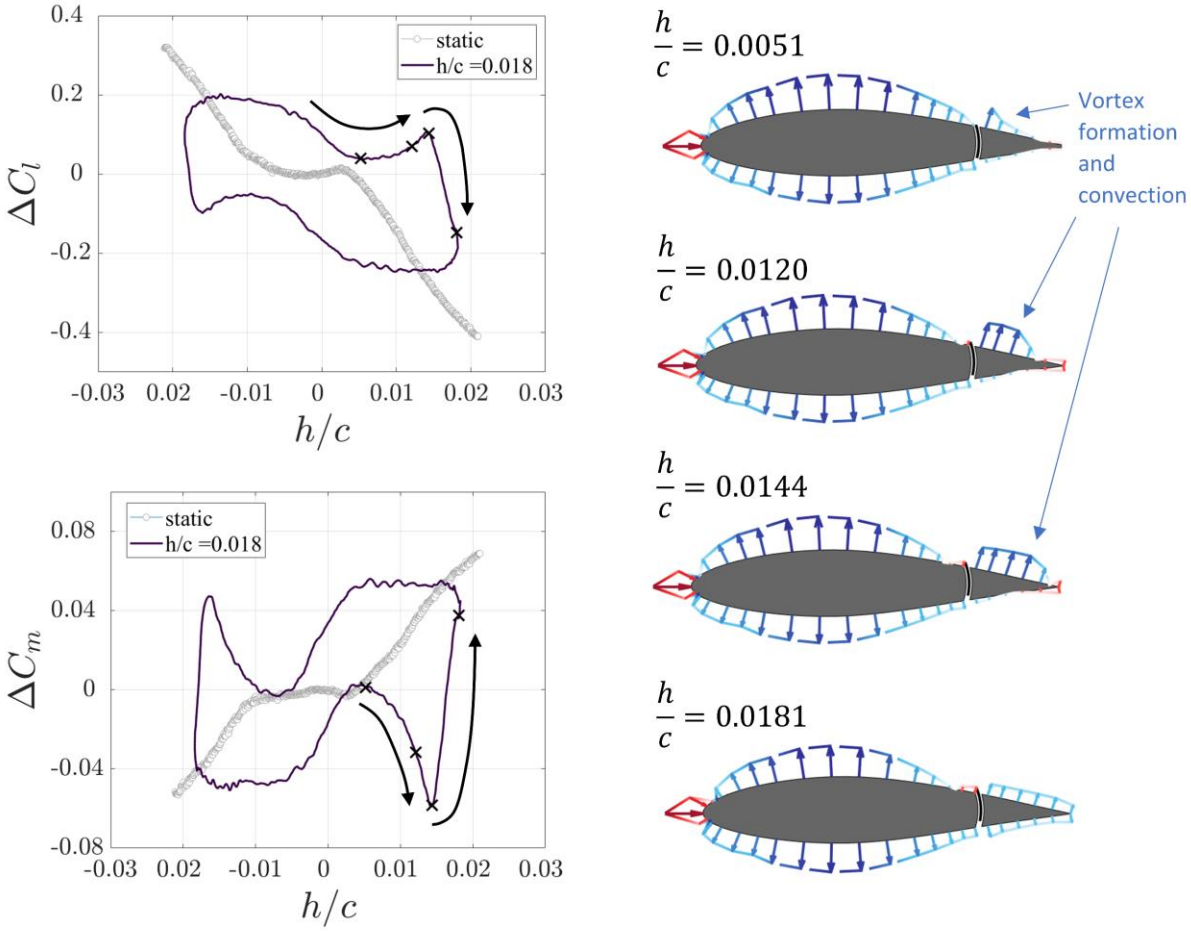

Figure 5: Aerodynamic loads and pressure data plotted at select deployment heights to reveal vortex formation – *k* =0.31, *h/c* = 0.018

As whirl flutter is esimated to occur between $k = 0.10$ to 0.20, vortex formation must be considered for any reduced-order model aiming to capture salient mini-tab flow physics. Though the vortex induced loads are directly opposed to the quasi-steady behavior, their effects are both rapid and substantial, and could be harnessed for high frequency disturbance rejection.

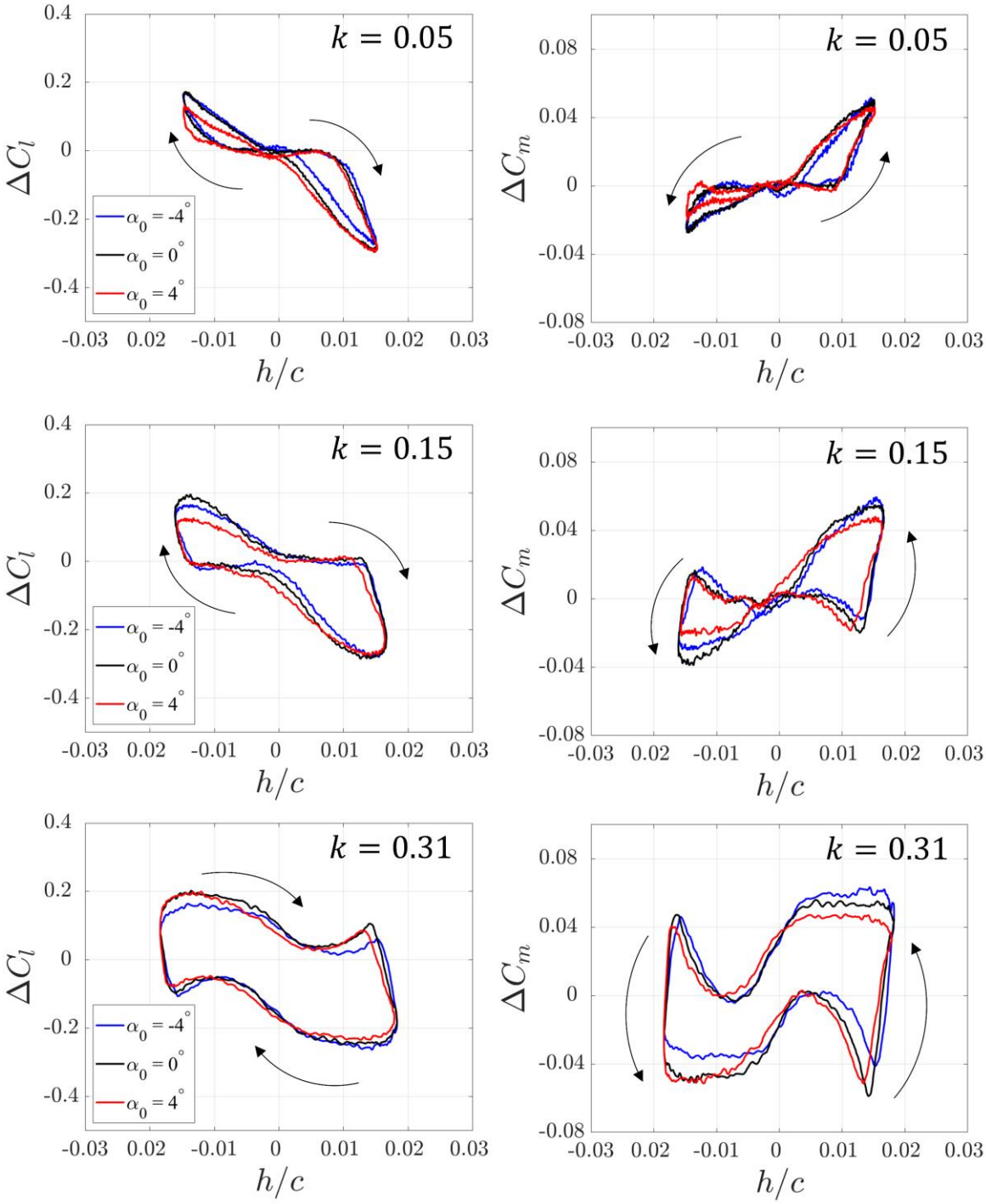

Figure 6: Dynamic mini-tab deployment at selected geometric angles of attack, α_0.

In the previous section, the mini-tab showed similar quasi-steady performance with moderate changes in geometric angle of attack. This observation is also held for dynamic performance, see Figure 6, where ΔC_l and ΔC_m are presented for $\alpha_0 = -4°, 0°$ and $+4°$ at the maximum deployment amplitude for each reduced frequency. Though minor variations exist across the α_0 range, the loops all display the same shape and salient features. This offers promise from a full-system modelling perspective, where the key mini-tab physics can be captured by an isolated model, regardless of wing states, around a given trim state.

The idea of mini-tab independence from wing kinematics is tested further through a series of dynamic motion tests,

1. A range of harmonic pitch, plunge and tab motion combinations were tested.
2. The wing kinematics from 1. were tested with no tab motion.
3. The tab motions from 1. were tested on a static wing at $\alpha_0 = 0°$.

If the mini-tab is insensitive to wing motion, then the aerodynamic loads from 1. can be estimated from the sum of 2. and 3. For this test, we consider small amplitude wing motions that are representative of flutter onset. Figure 7 presents the results of this study for select cases. Commanded motion profiles for pitch, plunge and mini-tab deployment for rows A, B and C are presented in Table 1. The pitch and plunge profiles aim to replicate flutter onset, where pitch tends to lead plunge by a phase of $\pi/2$, and are held constant for each case. Mini-tab deployment phase is altered by $\pi/2$ for each case. We consider here k = 0.15, as this is in the middle of the estimated XV-15 whirl flutter range of k = 0.1 to 0.2 [33]. Note that pitch motion occurs at the mid-chord and normalized period, t/T, is taken to be 0 at maximum pitch angle, α.

Table 1: Commanded harmonic motion parameters for Figure 7 (k=*0.15*)

	A	**B**	**C**
Pitch, $\boldsymbol{\alpha}$(°)	$2 \cdot \sin(ks + \pi/2)$	$2 \cdot \sin(ks + \pi/2)$	$2 \cdot \sin(ks + \pi/2)$
Plunge, $\boldsymbol{y/c}$	$0.01 \cdot \sin(ks)$	$0.01 \cdot \sin(ks)$	$0.01 \cdot \sin(ks)$
Mini-tab, $\boldsymbol{h/c}$	$0.0015 \cdot \sin(ks)$	$0.0015 \cdot \sin(ks + \pi/2)$	$0.0015 \cdot \sin(ks + \pi)$

Figure 7 presents the phase-averaged loads over 50 periods and demonstrates excellent agreement between the experiment and linearly combined wing and tab load responses. The pitching moment shape remains unaffected across all cases, as the airfoil's circulatory pitching moment repsonse to wing kinematics is small (note: the phase is shifted by $\pi/2$ – see Table 1). This clearly demonstrates, for the first time, mini-tab independence for flutter onset scenarios, and gives confidence in the develpoment of isolated mini-tab models, that are independent of wing states, for use in controller design.

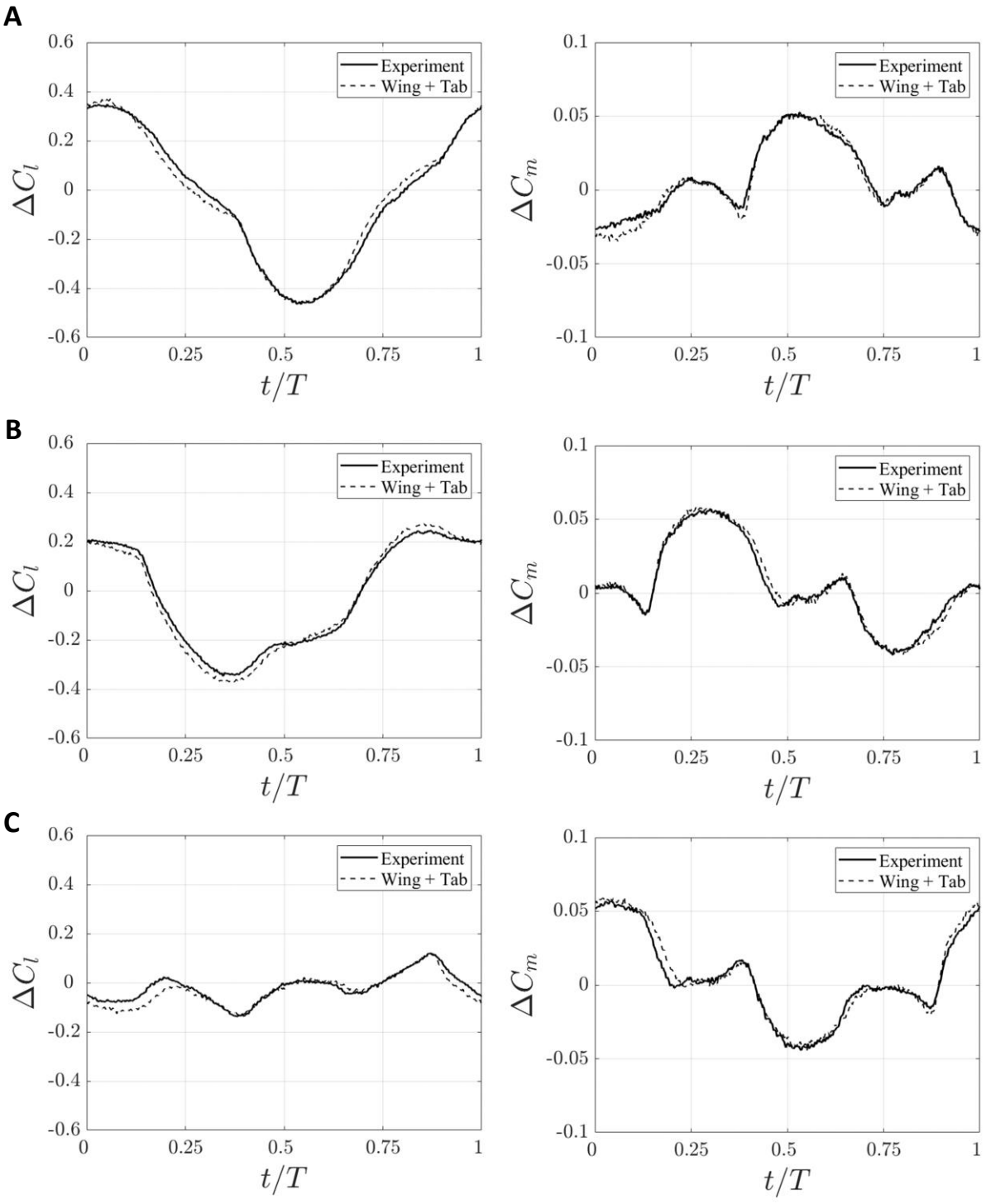

Figure 7: Loads for dynamic wing motion and mini-tab deployment, with linear superposition of isolated dynamic wing loads and dynamic tab loads at *k*=0.15.

IV. Modelling

It is evident from the results presented that linear analytical functions cannot capture the vortex induced effects on lift and pitching moment. We have opted to employ and modify an existing model introduced by Vieira and Maughmer [32] that is inspired by the classic Leishman-Beddoes [34] dynamic stall model. An overview of the model is provided here, and the reader is directed to [32] for a full description.

A. Mini-tab model outline

Fundamentally, mini-tab deployment on a generalized airfoil surface incurs changes in the lift and pitching moment coefficients, ΔC_l and ΔC_m. The associated aerodynamic response is dominated by circulatory and vortex-based components:

$$\Delta C_l = \Delta C_{l,circ} + \Delta C_{l,vtx} \tag{2}$$

$$\Delta C_m = \Delta C_{m,circ} + \Delta C_{m,vtx} \tag{3}$$

In deriving the component contributions, an indicial approach is favoured. Under this schema, effects of arbitrary motions over time – i.e., changes in angle of attack and unsteady inflow conditions - are approximated by a series of superimposed step responses. Eponymic indicial functions are then developed by fitting to time-domain aerodynamic responses. Vieira and Maughmer [32] demonstrated tab response estimates that agreed well with commercial CFD for mini-tab motions deployed on the lower surface only, with reduced frequencies, k, between 0.1 and 1.

Circulatory Effects

Assuming that the quasi-steady relationship between mini-tab position h and the lift augmentation $\Delta C_{l,qs}$ is known – either from CFD or experiment – such that $\Delta C_{l,qs}^n = f(h^n)$, at any discrete instance in time n, the circulatory lift for unsteady tab motion can be estimated. For mini-tabs inbound of the trailing-edge, $f(h^n)$ is nonlinear due to flow reattachment at small deployement heights. This nonlinearity is captured in the model through an effective quasi-steady mini-tab position $h_{l,qs}^n$. Consistent with [32], $\Delta C_{l,qs}^n$ is first normalized by the lift augmentation $\Delta C_{l,\mathrm{MT}}$ produced at a predetermined normalization height h_{MT}. Here we have taken the normalization height, h_{MT}, as $h/c = 0.015$.

$$\Delta C_{l,qs,norm}^{n} = \frac{\Delta C_{l,qs}^{n}}{\Delta C_{l,MT}} \tag{4}$$

Then, the static nonlinearity is mapped onto the effective tab position $h_{l,qs}^{n}$

$$h_{l,qs}^{n} = \Delta C_{l,qs,norm}^{n} h_{MT} \tag{5}$$

The indicial function for circulatory lift reported in [32] is a three-term exponential function resulting in three deficiency functions, D_{circ}, which impart effective lags on $h_{l,qs}^{n}$.

$$h_{l,eff}^{n} = h_{l,qs}^{n} - D_{1,circ}^{n} - D_{2,circ}^{n} - D_{3,circ}^{n} \tag{6}$$

where

$$D_{i,circ}^{n} = D_{i,circ}^{n} e^{\left(-\frac{b_{i,circ}\beta^{\gamma}\Delta s}{2}\right)} + A_{i,circ}\Delta h_{l,qs}^{n} e^{\left(-\frac{b_{i,circ}\beta^{\gamma}\Delta s}{2}\right)} \tag{7}$$

In discrete space, changes in the effective quasi-steady tab position are obtained according to $\Delta h_{l,qs}^{n} = h_{l,qs}^{n} - h_{l,qs}^{n-1}$, and the reduced time step $\Delta s = s^{n} - s^{n-1}$. $A_{i,circ}$ and $b_{i,circ}$ are coefficients tuned to fit the indicial functions to the forcing functions, and β^{γ} is a fluid compressibility correction factor for dynamics at Mach Number M. The Glauert-Prandtl factor, $\beta = \sqrt{1 - M^2}$, is the foundation of this correction. The circulatory lift is inferred from $h_{l,eff}^{n}$ such that

$$\Delta C_{l,circ}^{n} = \frac{h_{l,eff}^{n}}{h_{MT}} \Delta C_{l,MT} \tag{8}$$

The circulatory component of the pitching moment perturbation is obtained using the same procedure laid out for lift. The quasi-steady relationship between $h_{m,qs}^{n}$ and $\Delta C_{m,qs}^{n}$ is adopted in this case. Unique circulatory constants $A_{i,circ}$ and $b_{i,circ}$ must also be chosen to tune the pitching moment behavior - Vieira and Maughmer [32] note that only a two-term exponential is required to describe the pitching moment dynamics. The circulatory module of this model can therefore be thought of as a Hammerstein modelling paradigm, whereby linear perturbations are evaluated about a static nonlinear baseline.

Vortex Lift Effects

Beyond the critical tab deployment height h_{ini0}, a vortex is generated behind the mini-tab that grows and convects along the airfoil surface. Changes in lift due to vortex interactions with the airfoil surface

are included as the product of a vortex strength term $\Gamma_{l,vtx}$, and a convection function, which form the indicial vortex function V_f

$$\Delta C_{l,vtx}^{n} = \frac{V_f}{h_{MT}} \Delta C_{l,MT} \tag{9}$$

where

$$V_f = \Gamma_{l,vtx} \left[\sin\left(\frac{\pi(s - s_{ini})}{2T_{v,eff}} \right) \right]^{3/2} \tag{10}$$

$T_{v,eff}$ is a parameter indicating the time taken for the vortex to reach the trailing-edge once it has begun convecting. Since vortex generation is not instantaneous at the point where $h^n = h_{ini0}$, a time delay s_{ini} is built into V_f. This time delay is function of an effective mini-tab position $h_{ini,eff}^{n}$ which incorporates aerodynamic lags associated with the formation of the vortex.

$$h_{ini,eff}^{n} = h^n - D_{1,ini}^{n} \tag{11}$$

where

$$D_{i,ini}^{n} = D_{i,ini}^{n-1} e^{\left(-\frac{\Delta s}{T_{ini}}\right)} + \Delta h^n e^{\left(-\frac{\Delta s}{T_{ini}}\right)} \tag{12}$$

T_{ini} is a vortex formation time constant tuned to match the mini-tab behavior, and $\Delta h^n = h^n - h^{n-1}$. Thus, s_{ini} is defined as the instantaneous time s^n at the point where $h_{ini,eff}^{n} \geq h_{ini0}$.

One final effective parameter, $h_{te,eff}^{n}$, is established at this point to quantify the outstanding $T_{v,eff}$. For unsteady mini-tab deployment, further aerodynamic lags are associated with vortex convection towards the trailing-edge. Accordingly, $h_{te,eff}^{n}$ is as an abstraction of the effects of unsteady tab motion on the convection of the vortex. In the familiar notation

$$h_{te,eff}^{n} = h^n - D_{1,te}^{n} \tag{13}$$

where

$$D_{i,te}^{n} = D_{i,te}^{n-1} e^{\left(-\frac{\Delta s}{T_{te}}\right)} + \Delta h^n e^{\left(-\frac{\Delta s}{2T_{te}}\right)} \tag{14}$$

The constant T_{te} may be fit to produce behavior consistent with the airfoil being considered. Returning to the convection time characterization, $T_{v,eff}$ is determined by the effective mini-tab rate $h^{+n}_{te,eff}$

$$T_{v,eff} = A_{T_v}\left(h^{+}{}^{n}_{te,eff}\right)^{-n_{T_v}} \tag{15}$$

where

$$h^{+}{}^{n}_{te,eff} = \frac{h^{n}_{te,eff} - h^{n-1}_{te,eff}}{\Delta s} \tag{16}$$

Given that the strength of the vortex with respect to lift augmentation is correlated with its chordwise position on the airfoil surface, $\Gamma_{l,vtx}$ is also a function of $h^{n}_{te,eff}$

$$\Gamma_{l,vtx} = C_{vtx,l}\beta^{\gamma}\left(h^{n}_{te,eff} - h^{n}\right) \tag{17}$$

The peak strength of the vortex is dictated by the constant $C_{vtx,l}$, and compressibility effects are once again included through the Glauert-Prandtl correction, β^{γ}.

Arbitrary Vortex Dynamics

In the absence of an exact schematic in [32] for the application of V_f during arbitrary tab deployment, a generalised approximation has been developed in MATLAB as part of the present analysis. This approximation is extended to accommodate mini-tab motion on both the upper and lower surface of the airfoil where positive or negative h^n now imply mini-tab deployment on the upper or lower airfoil surface respectively. The upper airfoil surface vortex response implementation is visible in Figure 8.

This application is consistent with the qualitative vortex behavior described in [32], which asserts that (I) V_f should be set to zero during tab retraction, unless a previously induced vortex has not fully decayed, and (II) no conditions exist for the creation of a vortex other that the mini-tab crossing the h_{ini0} threshold. The vortex state parameter vtx_{st} indicates the status of any instantaneous vortices acting on the airfoil surface. At any point in the discrete simulation, vtx_{st} is an integer between 0 and 2. A value of 0 indicates that there is no active vortex, and the mini-tab is below h_{ini0}; a value of 1 indicates that a vortex is currently active; and a value of 2 indicates that the active vortex has fully decayed. Vortex arithmetic is initialized at different locations in the model space depending on the value of vtx_{st} as indicated by the red markers in Figure 8. An additional speed threshold $h^{+}{}^{n}_{thresh}$ is used to determine whether the tab is extending or retracting. In the original model $h^{+}{}^{n}_{thresh} = 0$, and

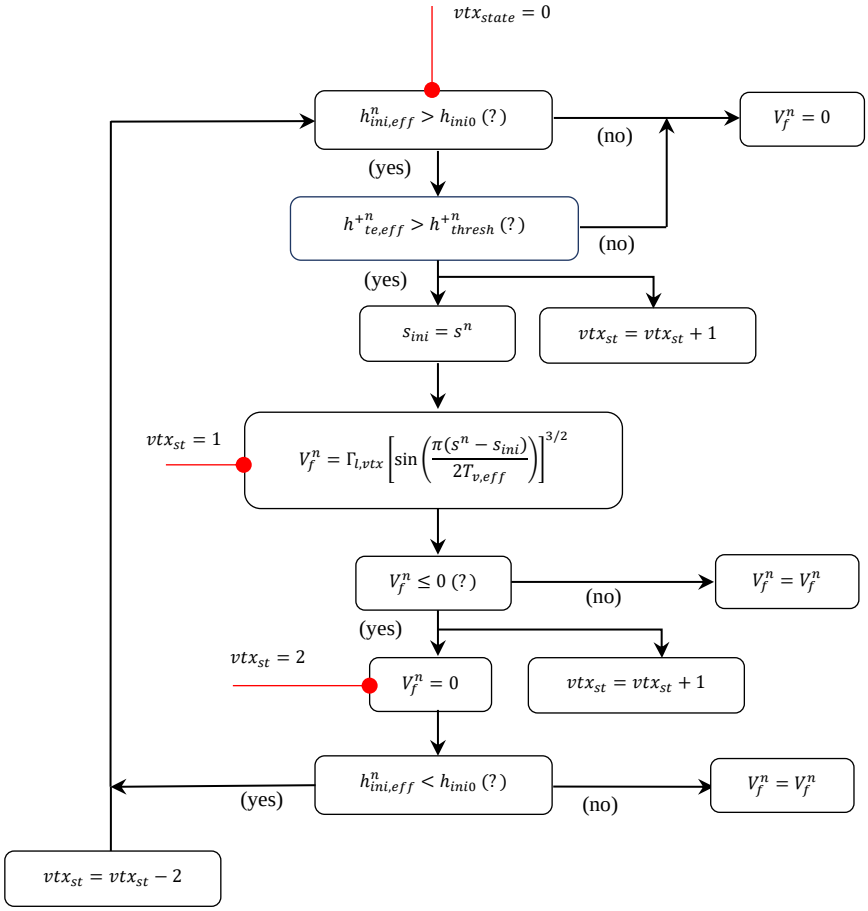

Figure 8: Vortex model flowchart

it will be shown later that this can be modified to better represent the vortex physics observed in the experimental results presented here.

The lower surface vortex model follows the same general structure but is implemented separately, because all checks against effective tab states must be modified to account for the inverse meaning of negative h^n in the context of lower surface deployment. More specifically, on the lower surface, a negative velocity h^{+n} corresponds to tab extension, and a positive h^{+n} corresponds to tab retraction, which represent an inversion of the upper surface behavior. To account for this, from top to bottom in Figure 8 the tab state checks must be replaced by (I) $h_{ini,eff} < -h_{ini0}$; (II) $h^{+n}_{te,eff} < -h^{+n}_{thresh}$; and (III) $h^n_{ini,eff} > -h_{ini0}$.

The analytical result is a set of vortex contributions $V_{f,lower}$ and $V_{f,upper}$ for lower and upper surface deployment that combine to form the full vortex behavior $V_{f,tot}$. The lift contribution is then evaluated such that

$$\Delta C_{l,vtx}^{n} = \frac{V_{f,tot}}{h_{MT}} \Delta C_{l,MT} \tag{18}$$

where

$$V_{f,tot} = V_{f,upper} + V_{f,lower} \tag{19}$$

Vortex moment contributions are a direct result of the vortex lift perturbation. Assuming the vortex lift acts through a moment arm, L_{arm}, about the quarter-chord of the wing, the vortex-based moment perturbation is

$$\Delta C_{m,vtx} = \Delta C_{l,vtx} \left(\frac{C_{vtx,m}}{C_{vtx,l}} \right) L_{arm} \tag{20}$$

B. Model modification

When tuning the vortex module, it became apparent that it was lacking a key feature present in the experimental data – that is the dependence of vortex initiation on both critical tab height *and* tab rate. This is explored in Figure 9, where the chord normal force contribution of the vortex is assessed. The analysis focusses on the presssure sensors aft of the tab, on the upper and lower surface independently (Figure 9a), and extracts

$$\Delta C_N = \underset{min}{max} \left(C_N - C_{N,static} \right) \tag{21}$$

where C_N is the chord normal force during vortex passage, and $C_{N,static}$ is the chord normal force of the quasi-static pressure at the correspinding instantaneous tab height. The *max* and *min* depend on the sign of tab deployment – i.e. the upper or lower surface. For example, deployments on the upper suface will extract the *max* of the arugment in equation (21), as the vortex induces a positive chord normal force. The relative vortex normal forces, ΔC_N, are plotted against $k\,h/c$, which is a proxy for max tab deployment rate. The data collapses well for the range of h/c and k. At low kh/c (Figure 9b), the data are clustered close to $\Delta C_N = 0$, indicating no vortex formation. As kh/c increases, ΔC_N displays a monotonic increase/decrease from around $k\,h/c > 0.001$ for the upper and lower surface regions respectively. The effect of amplitude is also evident in Figure 9c, where the markers are colored by tab height. The lowest amplitudes show no appreicable vortex formation, and again highight the critical tab height needed for flow separation.

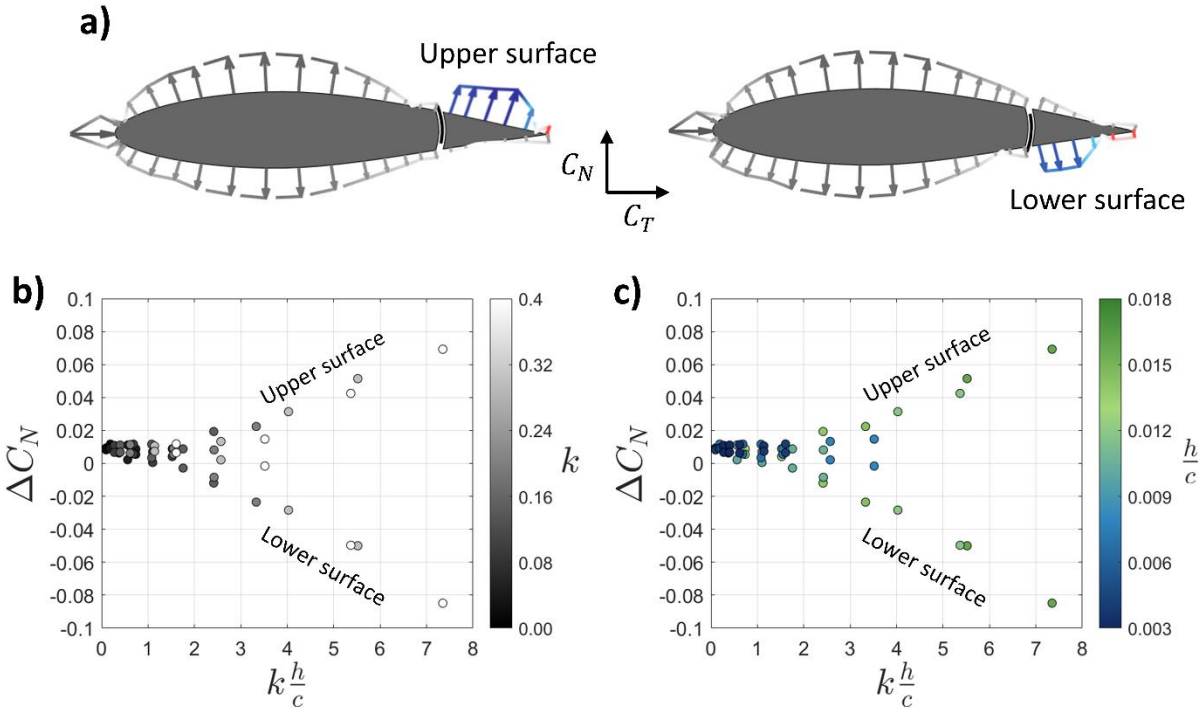

Figure 9: a) Pressure of aft-tab region, b) Chord-normal force of the tab vortex colored by *k* and c) colored by *h/c*.

In the baseline model the vortex initiates at all non-zero tab deployment rates - provided the critical tab height, h_{ini0}, is exceeded during extension - and the amplitude of the vortex disturbance is proportional to the tab deployment rate. To illustrate this, Figure 10a plots $\underset{max}{min}\,(\Delta C_{l,vtx})$ for a range of reduced frequencies at $h/c = 0.0018$ – shown by the black dashed line. The vortex strength, Γ_{vtx}, displays a near linear increase with tab rate, kh/c, however the vortex strength is non-zero at low tab rates, $kh/c < 0.001$, which is in contrast with the experimental data. To rectify this, we employ two simple corrections. The first is to include a tab rate threshold, $h^+_{thresh} = 0.001$ as indicated in Figure 10a. The second is to take the vortex strength amplitude at h^+_{thresh} and subtract it from the vortex strength equation, such that

$$\Gamma_{l,vtx} = C_{vtx,l}\beta^{\gamma}\left(h^{n}_{te,eff} - h^{n}\right) - \Gamma_0 \tag{22}$$

where Γ_0 in this case has been taken as a best fit constant to produce smooth vortex initiation behavior across a range of tab amplitudes – blue line in Figure 10a. A comparison against the experimental vortex normal force, ΔC_N, is presented in Figure 10b where the model shows reasonable agreement

with trends in the data across different tab rates and amplitudes. It is worth noting that $\Delta C_N \approx \Delta C_{l,vtx}$, as the extraction of ΔC_N can only approximate the true vortex induced load. Nevertheless, it provides verification for the proposed correction and a method for tuning the h^+_{thresh} and Γ_0 constants in the model.

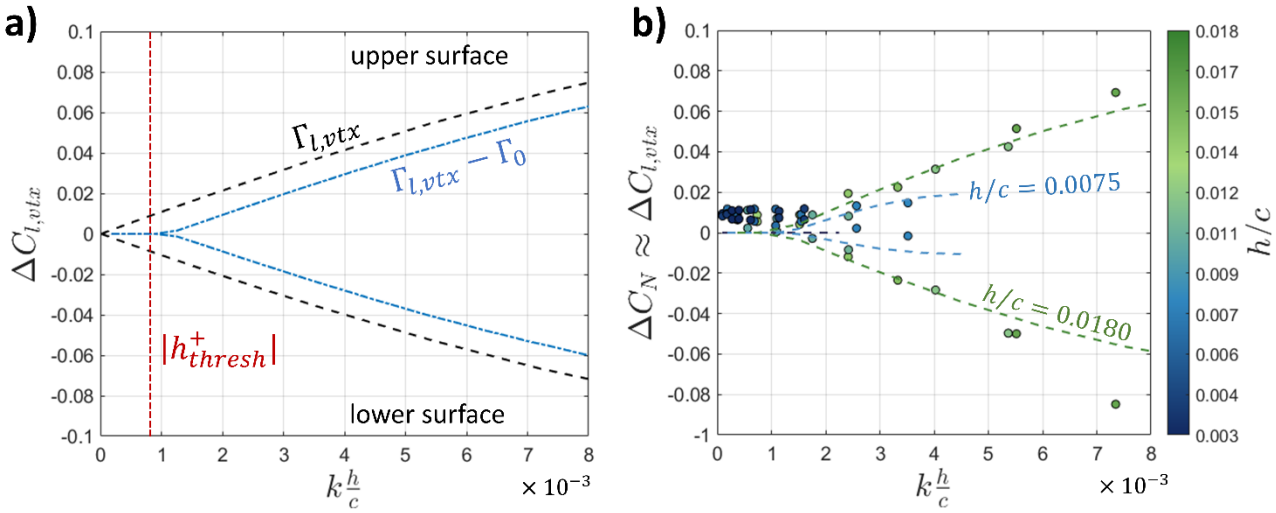

Figure 10: a) Vortex induced lift amplitude for baseline and modified model, b) comparison of modified model to experimental vortex lift.

C. Comparison to Experimental Data

With the vortex module modified to exhibit more representative vortex intiation, the full model was tuned to select cases of experimental data. The following tuning process consisted of a series of local optimizations for efficient minimisation of the root mean squared error between the model prediction and the experimental data. Although a single, global optimizer run could also be used here, a local approach was favored for speed. The loss function took the form

$$Loss = \frac{\sum_{i=1}^{N}\left(\hat{C}_i^e - \hat{C}_i^m\right)^2}{N} \tag{23}$$

where $\hat{C}_i^e$ is the normalized experimenal aerodynamic coefficient for data point i, $\hat{C}_i^m$ is the normalized model prediciton, and N is the total number of data points. The aerodynamic coefficients were normalized by

$$\hat{C} = \frac{C - \min\left(C^e\right)}{\max(C^e) - \min\left(C^e\right)} \tag{24}$$

where the minimum and maximum values of the experimental data are used for normalization of both the experimental and model values. The optimization process was as follows:

1. Tune the circulatory constants for the lift at $k = 0.1$ using the loss function

$$Loss = \frac{\sum_{i=1}^{N}\left(\hat{C}_{l,i}^{e} - \hat{C}_{l,i}^{m}\right)^2}{N} \tag{25}$$

2. Tune the circulatory constants for the pitching moment at $k = 0.1$ using the loss function

$$Loss = \frac{\sum_{i=1}^{N}\left(\hat{C}_{m,i}^{e} - \hat{C}_{m,i}^{m}\right)^2}{N} \tag{26}$$

3. Tune the vortex constants for both the lift an pitching moments at $k = 0.15$ using the circulatory constants from 1 and 2, with the loss function

$$Loss = \frac{\sum_{i=1}^{N}\left(\hat{C}_{l,i}^{e} - \hat{C}_{l,i}^{m}\right)^2}{N} + \frac{\sum_{i=1}^{N}\left(\hat{C}_{m,i}^{e} - \hat{C}_{m,i}^{m}\right)^2}{N} \tag{27}$$

4. Tune all model constants across the frequency range $k = 0.05, 0.10, 0.15$ using the circulatory and vortex constants as an initial condition, through the loss funciton

$$Loss = \frac{\sum_{i=1}^{N}\left(\hat{C}_{l,i}^{e} - \hat{C}_{l,i}^{m}\right)^2}{N} + \frac{\sum_{i=1}^{N}\left(\hat{C}_{m,i}^{e} - \hat{C}_{m,i}^{m}\right)^2}{N} \tag{28}$$

Steps 1-3 provide step 4 with an improved initial condition. By tuning at a moderate reduced frequency of $k = 0.1$, before any appreciable vortex influence on the aerodynamic loads, the lift and pitching moment circulation constants could be tuned independently (steps 1 and 2), yielding a reasonable starting point for subsequent steps. A tuning frequency of $k = 0.15$ for the vortex model displayed the best overall performance across the reduced frequency range $k = 0.05$ to 0.31. Higher values of k were trialled for tuning, but this degraded overall model performance. As will be shown later, this is likely due to the model's inability to capture additional flow physics during strong vortex shedding events. Finally, all constants were tuned over moderate frequencies ($k = 0.05$, 0.10, 0.15) using the optimized constants from steps 1 to 3 as an intial condition. All optimization runs were performed in MATLAB using the active-set algorithm in *fmincon()*. As the Mach number is small, the the Glauert-Prandtl factor was set to $\beta = 1$.

The circulatory constants that produced the best overall performance are shown in Table 2. As reccomended by Viera and Maughmer [32], different b_i constants were used for mini-tab extension and retraction. Note that the optimizer settled on a single deficiency function for the pitching moment, and as such A_2 and b_2 have been removed.

Table 2: Optimized circulatory model constants.

Lag Type	A_1	A_2	A_3	b_1	b_2	b_3
Lift extension	0.059	1.216	0.106	1.547	1.004	0.224
Lift retraction				1.208	0.991	0.140
Moment extension	1.995	--	- -	1.766	--	- -
Moment retraction				1.424		

The vortex constants are shown in Table 3. Two separate vortex initiation tab heights, $h_{ini,0,u}$ and $h_{ini,0,l}$, are defined for the upper and lower surfaces respectively, based on observations in the data. For simplicty, the remaining vortex constants were held the same for upper and lower surface vortex formation. Further work could investigate a separate set of constants for each surface, and any benefits that may yield.

Table 3: Optimized vortex model constants

T_{ini}	$h_{ini,0,u}$	$h_{ini,0,l}$	h^+_{thresh}	T_{te}	A_{Tv}	n_{Tv}	$C_{vtx.l}$	$C_{vtx.m}$	Γ_0
1.00	0.0025	0.0040	0.001	0.336	0.00052	-1.48	3.40	15.71	-0.00075

A comparsion of the model to select experimental data is shown in Figure 11. At k = 0.05, the model shows good agreement with the experiment. Here $kh/c < h^+_{thresh}$, so the vortex model remains inactive and the loads responses consist of the ciculatory component only. When k is increased to 0.15, the model captures the correct loop shapes through the summation of the circulatory and vortex induced loads. The model begins to fall out of agreement at k = 0.31, though the magnitude of the vortex induced loading is well captured. Particular diagreement is noted in the pitching moment prediction, where the tab begins to retract after the votex has decayed. The model cannot capture the plataeu at $\Delta C_m = 0.05$ as this artifact is not present in the underlying quasi-static response. It points towards additional mechanisms triggered by significant tab vortex formation and shedding. The passing of the coherent vortical disturbance over the trailing-edge would trigger a trailing-edge vortex of opposite sign that would subsequently interact with the upstream separated flow - reminiscent of mechanisms found in the dynamic stall phenomenon [35]. These mechanisms are not captured in the existing model structure. Vieira and Maughmer [32] noted increasing disagreement at higher reduced frequencies, and they postulated the root of this could be unmodelled, secondary vortices.

Nevertheless, the current modified model performs well in the estimated frequency range of XV-15 whirl flutter (k = 0.1 to 0.2 [33]).

To validate the optimized constants, the model's transient performance was assessed through mini-tab ramp-hold functions. The ramp demands were defined as a deployment height of h/c = -0.015 to 0.015, and h/c = 0.015 to -0.015, at reduced deployment rate of

$$K = \frac{\dot{h}}{c}\frac{c}{2U_\infty} \tag{29}$$

where $\dot{h}/c$ is a constant deployment rate demand (s^{-1}). Experimental results show the ensemble average of 15 repeats at K = 0.016 and 0.025 (Figure 12). To put these depoyment rates into context with the periodic cases, K = 0.0015 and 0.0031 yield a kh/c equivalent of 0.0030 and 0.0062 respectively (see Figure 10) . Once again, the model shows good agreement with the experimental lift and pitching moment in terms of the circulatory component and vortex contribution – which can be observed just after $h/c = 0$.

Although the optimized constants are specific to the system presented in this study, and would require retuning for different flight hardware (i.e. airfoil, mini-tab geometry and mini-tab chordwise position), such a model is still useful in the aircraft design stage - analogous to similar semi-empirical models frequently used in industrial design [34]. Reynolds number and compressibility effects will have some impact on the generalizability of the model constants to different flight speeds. However, as the mini-tab flow physics is goverened by a fixed flow separation point and coherent vortex formation, the Reynolds number would likely have to change by an order of magnitude to have a significant impact on the loads [36]. The modelling approach here is intended to faclitate controller design around the critical whirl flutter velocity and is expected to be valid across a practical Reynolds number range. In addition, Viera and Maughmer [32] were able to efficiently capture compressibility effects by scaling the indicial constants to account for changes to the vortex magnitude and circulatory lags with satisfactory results.

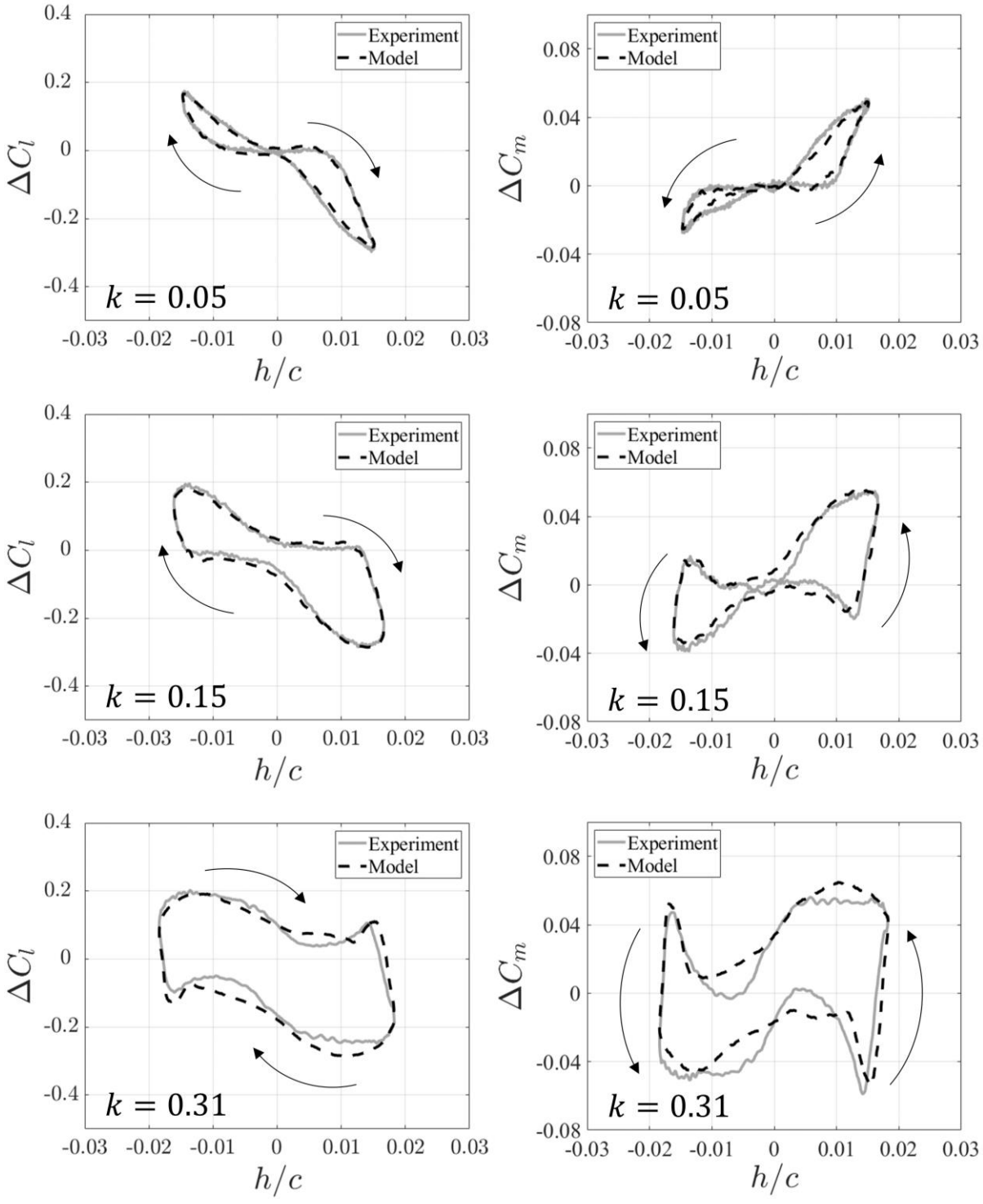

Figure 11: Model comparison with vortex initiation modification against periodic experimental data

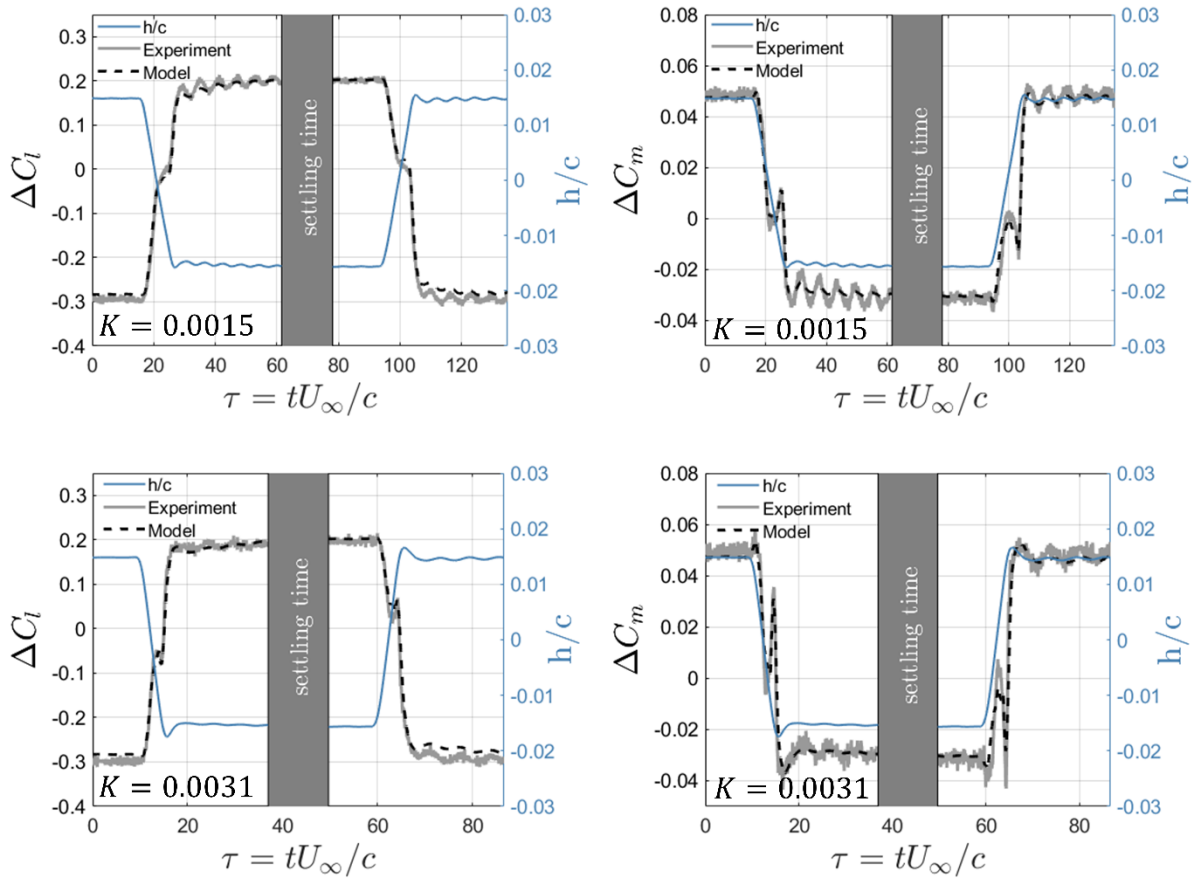

Figure 12: Model comparison against transient experimental data

Conclusions

This study has experimentally investigated the performance of a mini-tab (micro tab/flow fence) device for active flow control under static and dynamic wing conditions. This was achieved using The University of Bath's novel Test Rig for Unsteady aeroDYnamics (TRUDY), which can provide high-frequency, high-amplitude airfoil/wing motion in three degrees of freedom, whilst dynamically deploying the mini-tab for load augmentation.

Under quasi-steady conditions, the mini-tab exhibited non-linear performance caused by flow reattachment behind the tab at low deployment heights. When the mini-tab was sinusoidally deployed, the aerodynamic loads displayed small hysteresis around the quasi-steady response at low reduced frequencies ($k = 0.05$). At mid to high reduced frequencies (k = 0.15 to 0.31), significant undulations emerged in the load responses that directly opposed the quasi-steady performance. Pressure measurements revealed this to be caused by a vortex that forms and propagates downstream of the tab, the initiation of which depends on both deployment frequency and height.

It was demonstrated, for the first time experimentally, that the mini-tab dynamic performance is insensitive to unsteady airfoil motion at representative flutter onset conditions. Dynamic mini-tab deployments were performed on a pitching and plunging airfoil at k = 0.15 and compared with the combination of corresponding isolated wing and tab motion signals. The two showed excellent agreement and give confidence in the use of stand-alone mini-tab models for full-system control.

Finally, an existing mini-tab model was extended to capture vortex formation on the upper and lower airfoil surfaces and modified to incorporate mini-tab rate-dependence on vortex initiation, as observed in the experimental data. The model demonstrated good loads prediction at low to mid reduced frequencies (k = 0.05 to 0.15) but displayed some disagreement at k = 0.31. This points towards the development of model extensions to capture additional flow physics present at higher reduced frequencies.

The work outlined in this paper lays important foundations for continued mini-tab development, and future efforts can be placed on their incorporation into control systems. Though the loads responses display significant non-linearities due to vortex formation, the rapid and significant loads they produce could be harnessed for control and disturbance rejection. The mutual interaction of the separated and vortical mini-tab flow with conventional control surfaces (flaperons and ailerons) remains an open question and will need to be considered for a more comprehensive loads model.

Acknowledgements

The authors acknowledge the Engineering and Physical Sciences Research Council (EPSRC) Grant No. EP/S011382/1. Data is available upon request. Thank you to George Smith for his contributions to Figure 1.

References

[1] Frost and Sullivan (2019). Analysis of Urban Air Mobility and the Evolving Air Taxi Landscape. Retrieved from https://store.frost.com/analysis-of-urban-air-mobility-and-the-evolving-air-taxi-landscape-2019.html

[2] Guruswamy, G. "Dutch-Roll Stability Analysis of an Air Mobility Vehicle Using Navier-Stokes Equations," AIAA Journal, Vol. 59, No. 10, October 2021. doi: 10.2514/1.J060055.

[3] Brown, R. "Are eVTOL aircraft inherently more susceptible to the vortex ring state than conventional helicopters?" Technical Paper, Sophrodyne Aerospace, 2022.

[4] Koch, C. "Parametric whirl flutter study using different modelling approaches," CEAS Aeronautical Journal, 13:57-67, 2022. doi: 10.1007/s13272-021-00548-0.

[5] Chen, H., and Chen, B., “Lift Enhancement of Tiltrotor Wing Using a Gurney Flap,” International Journal of Aerospace Engineering, 1245484, 2022. doi: 10.1155/2022/1245484.

[6] Turner, H. L., and Drinkwater III, F. J., “Some Flight Characteristics of a Deflected Slipstream V/STOL Aircraft,” Technical Report, NACA TN D-1891, 1963.

[7] Proenca A.R., Prince S.A., Banks-Davies L., and Garry K.P., “Experimental evaluation of a passive flow-control device for a tiltrotor aircraft,” ICAS 2022: 33rd Congress of the International Council of the Aeronautical Sciences, 4-9 September 2022, Stockholm, Sweden.

[8] Kim, T.S.; Lim, J.H.; Shin, A.J.; Kim, D.H. “Structural design optimization of a tiltrotor aircraft composite wing to enhance whirl flutter stability,” Composites Structures, 2013, 95, 283–294. doi: 10.1016/j.compstruct.2012.08.019.

[9] Stodieck, O.; Cooper, J.; Weaver, P.M.; Kealy, P. “Optimization of tow-steered composite wing laminates for aeroelastic tailoring” AIAA Journal 2015, 53, 2203–2215. doi: 10.2514/1.J053599.

[10] Hathaway, E. L., and Gandhi, F., “Tiltrotor Whirl Flutter Alleviation Using Actively Controlled Wing Flaperons,” AIAA Journal, Vol. 44, No. 11, 2006, pp. 2524-2534. doi: 10.2514/1.18428.

[11] Gardner, A. D., Richter, K., Mai, H., and Neuhaus, D., “Experimental investigation of high-pressure pulsed blowing for dynamic stall control,” CEAS Journal, 2014, 5:185-198. doi: 10.1007/s13272-014-0099-y.

[12] Deem, E. A., Cattafesta III, L. N., Hemati, M. S., Zhang, H., Rowley, C., and Mittal, R., “Adaptive separation control of a laminar boundary layer using online dynamic mode decomposition,” Journal of Fluid Mechanics, 2020, vol. 903. doi: 10.1017/jfm.2020.546.

[13] Lombardi, A. J., Bowles, P. O., and Corke, T. C., “Closed-Loop Dynamic Stall Control Using a Plasma Actuator,” AIAA Journal, Vol. 51, No. 5, 2013. doi: 10.2514/1.J051988.

[14] Chen, Z., Shi, Z., Chen, S., Liao, X., and Mei, Y., “Active flutter suppression on a flexible wing via leading-edge blowing and circulation control,” Physics of Fluids, 35, 094106, 2023. doi: 10.1063/5.0162013.

[15] Khalil, K., and Bauknecht, A., “Fluidic Flow Control Devices for Gust Load Alleviation,” Journal of Aircraft, 2024. doi: 10.2514/1.C037503.

[16] Kroo, I. M., and Bieniawski, S., “Flutter Suppression Using Micro-Trailing Edge Effectors,” 44th AIAA/ASME/ASCE/AHS Structures, Structural Dynamics and Materials Conference, April 2003, Virginia.

[17] Yang, J., Yang, H., Wang, X., ad Li, N., “Experimental Study of a Gurney Flap on a Pitching Wind Turbine Airfoil under Turbulent Flow Conditions,” Journal of Marine Science and Engineering, 2022, 10, 371. doi: 10.3390/jmse10030371.

[18] Johnson, W., “Dynamics of Tilting Proprotor Aircraft in Cruise Flight,” NASA TN D-7677, 1974.

[19] Maisel, D. M., Giulianetti, D. J., and Dugan, D. C., *The History of The XV-15 Tilt Rotor Research Aircraft*: *From Concept to Flight*, Vols. NASA SP-2000-4517, Washington DC: NASA History Division, 2000.

[20] van Aken, J., M., “Alleviation of whirl-flutter on a joined-wing tilt-rotor aircraft configuration using active controls,” *Proceedings of the 47th Annual AHS Forum*, The American Helicopter Society, Alexandria, VA, 6–8 May 1991.

[21] Nasu, K.-i., “Tilt-Rotor Flutter Control in Cruise Flight,” NASA TM 88315, Dec. 1986.

[22] Dong, L., and Li, Q., “Whirl Flutter Suppression of Tiltrotor Aircraft using Actively Controlled Aileron,” NASA-CR-196103, American Helicopter Society, 1991. doi: 10.3390/aerospace9120795.

[23] Heathcote, D., Gursul, I., and Cleaver, D.J., “Dynamic Deployment of a Mini-tab for Aerodynamic Load Control”, Journal of Aircraft, Vol. 57, No. 1, January–February 2020, pp. 41-6. doi: 10.2514/1.C035556.

[24] Bull, S., Chiereghin, N., Cleaver, D. J., and Gursul, I., “Novel Approach to Leading-Edge Vortex Suppression,” AIAA Journal, Vol 58, Issue 10, 2020. doi: 10.2514/1.J059444.

[25] Cooperman, A., M., Chow, R., and van Dam, C., P., “Active Load Control of a Wind Turbine Airfoil Using Microtabs,” Journal of Aircraft, Vol 50, No 4, 2013. doi: 10.2514/1.C032083

[26] Bach, A. B., 2016. Gurney Flaps and Micro- Tabs for Load Control on Wind Turbines. Ph.D. Dissertation, Technische Unversitat Berlin, Berlin.

[27] Kinzel, M., P., Maughmer, M., D., “Miniature Trailing-Edge Effectors for Rotorcraft Performance Enhancement,” Journal of the American Helicopter Society, Vol 52, No 2, 2007, pp. 146-158(13). doi: 10.4050/JAHS.52.146.

[28] Kinzel, M., P., Maughmer, M., D., and Duque, E., P., N., “Numerical Investigation on the Aerodynamics of Oscillating Airfoils with Deployable Gurney Flaps”, AIAA Journal, 48 (7), 2010. doi: https://doi.org/10.2514/1.J050070

[29] Matalanis., C., G., Wake, B., E., Opoku, D., Min, B., Y., Yeshala, N., and Sakar, L., “Aerodynamic Evaluation of Miniature Trailing-edge Effectors for Active Rotor Control,” Journal of Aircraft, Vol. 48, No. 3, 2011. doi: 10.2514/1.C031191.

[30] Tang, D., and Dowell, E., H., “Aerodynamic Loading for an Airfoil with an Oscillating Gurney Flap,” Journal of Aircraft, Vol. 44, No. 4, 2007. doi: 10.2514/1.26440.

[31] Bull, S. C., 2020. “Unsteady Aerodynamics of Wings in Extreme Conditions,” Ph.D. Dissertation, Department of Mechanical Engineering, The University of Bath, Bath, England, U.K.

[32] Vieira, B., A., O., and Maughmer, M., D., “Unsteady Aerodynamic Model for Deployable Gurney Flaps Based on Inidicial Concepts,” Journal of Aircraft, Vol. 54, No. 4, 2017. doi: 10.2514/1.C033960.

[33] Acree, C., W., Peyran, R., J., and Johnson, W., “Rotor Design Options for Improving XV-15 Whirl-Flutter Stability Margins”, NASA/TP-2004-212262, 2004.

[34] Leishman G. J. and Beddoes T. S., “A Semi-Empirical Model for Dynamic Stall,” Journal of the American Helicopter Society, Vol. 34, No. 3, 1989, pp. 3–17.

[35] Mulleners, K., and Raffel, M., “The onset of dynamic stall revisited,” Experiments in Fluids, Vol 52, 2012, pp.779–793. doi: 10.1007/s00348-011-1118-y.

[36] Eldredge, J. D., and Jones, A. R., “Leading-Edge Vortices: Mechanics and Modeling,” Annual Review of Fluid Mechanics, 2019, 51:75-104. doi: 10.1146/annurev-fluid-010518-040334.